PROTEINS
STRUCTURE ■ FUNCTION ■ BIOINFORMATICS

Toward decrypting the allosteric mechanism of the ryanodine receptor based on coarse-grained structural and dynamic modeling

Wenjun Zheng*

Department of Physics, State University of New York at Buffalo, Buffalo, New York 14260

ABSTRACT

The ryanodine receptors (RyRs) are a family of calcium (Ca) channels that regulate Ca release by undergoing a closed-to-open gating transition in response to action potential or Ca binding. The allosteric mechanism of RyRs gating, which is activated/regulated by ligand/protein binding >200 Å away from the channel gate, remains elusive for the lack of high-resolution structures. Recent solution of the closed-form structures of the RyR1 isoform by cryo-electron microscopy has paved the way for detailed structure-driven studies of RyRs functions. Toward elucidating the allosteric mechanism of RyRs gating, we performed coarse-grained modeling based on the newly solved closed-form structures of RyR1. Our normal mode analysis captured a key mode of collective motions dominating the observed structural variations in RyR1, which features large outward and downward movements of the peripheral domains with the channel remaining closed, and involves hotspot residues that overlap well with key functional sites and disease mutations. In particular, we found a key interaction between a peripheral domain and the Ca-binding EF hand domain, which may allow for direct coupling of Ca binding to the collective motions as captured by the above mode. This key mode was robustly reproduced by the normal mode analysis of the other two closed-form structures of RyR1 solved independently. To elucidate the closed-to-open conformational changes in RyR1 with amino-acid level of details, we flexibly fitted the closed-form structures of RyR1 into a 10-Å cryo-electron microscopy map of the open state. We observed extensive structural changes involving the peripheral domains and the central domains, resulting in the channel pore opening. In sum, our findings have offered unprecedented structural and dynamic insights to the allosteric mechanism of RyR1 via modulation of the key collective motions involved in RyR1 gating. The predicted hotspot residues and open-form conformation of RyR1 will guide future mutational and functional studies.

Proteins 2015; 00:000–000.

Key words: elastic network model; normal mode analysis; flexible fitting; ryanodine receptor; channel gating; hotspot residues.

INTRODUCTION

Calcium (Ca) signaling is critically involved in a diversity of physiological processes such as the excitation-contraction coupling in skeletal and cardiac muscles. As a key Ca channel that regulates Ca concentration, ryanodine receptors (RyRs)[1,2] undergo a closed-to-open gating transition to release Ca from the sarcoplasmic reticulum (SR) in response to an action potential that activates the voltage-gated calcium channels (Ca_v) which subsequently activate RyRs via physical interactions between Ca_v and RyRs.[3] RyRs can also be activated by Ca which may bind to the EF hand (EFH) domain or other Ca-binding sites. [4–8] RyRs are subject to complex regulations by various agents including ATP, Mg, phosphorylation, redox potential, and via interactions with other proteins such as FK506 binding proteins (FKBP)[9] and calmodulin (CaM),[10] which involve various functional domains of RyRs.[11] Remarkably, the binding sites for various activating/regulatory agents are separated from the channel gate by as much as >200 Å in RyR1,[2] highlighting the importance of an allosteric coupling mechanism yet to be decrypted.

Additional Supporting Information may be found in the online version of this article.

Grant sponsor: American Heart Association; Grant number: 14GRNT18980033; Grant sponsor: National Science Foundation; Grant number: 0952736.

*Correspondence to: Wenjun Zheng, 239 Fronczak Hall, Buffalo, NY 14260. E-mail: wjzheng@buffalo.edu

Received 10 August 2015; Revised 9 October 2015; Accepted 14 October 2015
Published online 00 Month 2015 in Wiley Online Library (wileyonlinelibrary.com). DOI: 10.1002/prot.24951

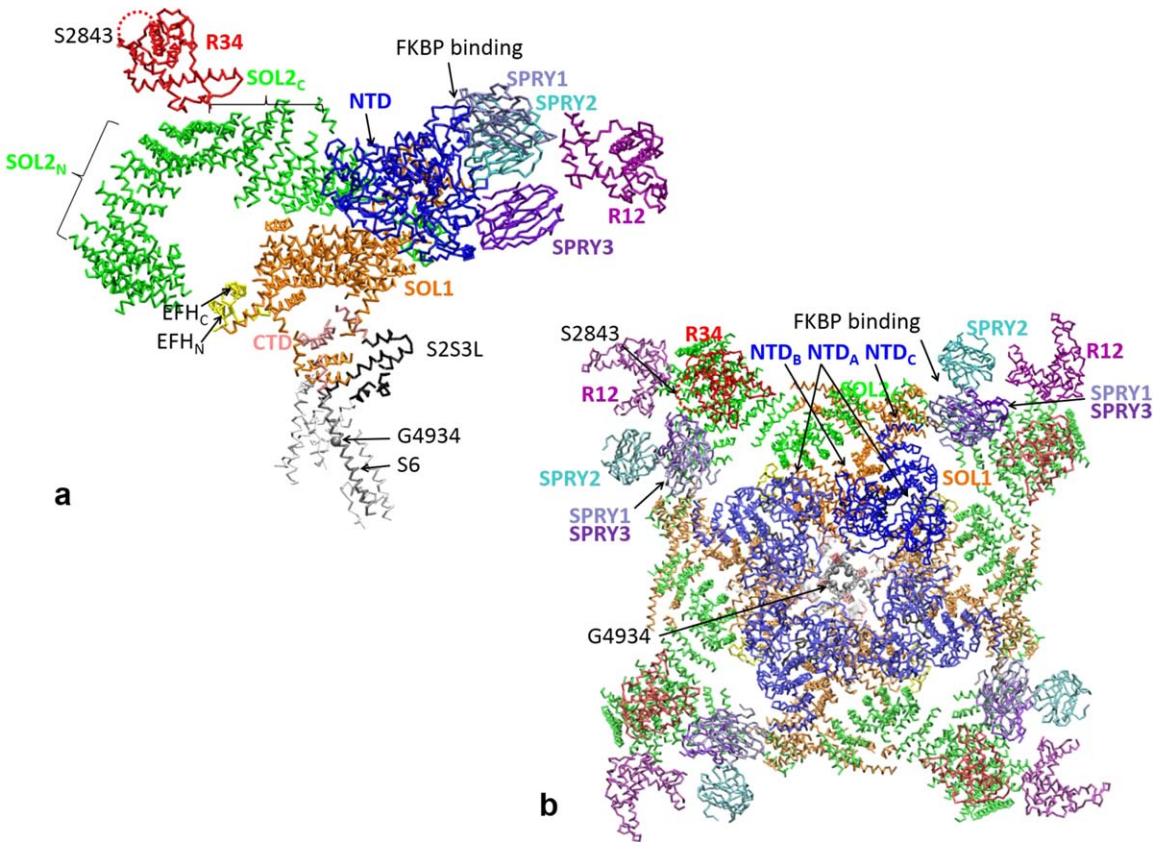

Figure 1

Structural architecture of RyR1 in the closed state (PDB code: 4UWA): (**a**) the side view showing the following domains for a representative subunit: NTD (blue), SOL1 (orange), SPRY1 (ice blue), R12 (purple), SPRY2 (cyan), SPRY3 (violet), $SOL2_N$ and $SOL2_C$ (green), R34 (red), S2S3L (black), CTD (pink), and the rest of TMD (gray). Residue G4934 at the channel gate is shown as a gray sphere. The following key functional sites and structural elements are labeled: two Ca-binding EF hand motifs (EFH_N and EFH_C), S6 helix, phosphorylation site S2843, and FKBP-binding site. (**b**) The top view of entire RyR1 tetramer with the same color scheme as panel (a).

Among three isoforms of RyRs in mammals, RyR1 is abundant in skeletal muscle and RyR2 is predominant in cardiac myocytes. More than 500 mutations in RyR1 and RyR2 have been linked to human diseases including malignant hyperthermia, central core disease, and various heart disorders,[12–14] making RyRs a potential therapeutic drug target.[15] While several models for disease mechanisms were proposed and debated [see reviews in Ref. 12 and [16]], the molecular mechanisms underlying the activation and regulation of RyRs in health and disease remain largely unknown for the lack of high-resolution structures for RyRs. Thanks to great efforts in structural biology, RyRs were visualized at $\geq$10 Å resolutions by cryo-electron microscopy (cryo-EM),[17–23] and the crystal structures of the N-terminal fragments and the phosphorylation domain of RyRs were solved.[1,2] Nevertheless, it remains highly challenging to solve the entire structure of RyRs at high resolution owning to their enormous size ($\sim$2.2 MDa and >20,000 residues) and high flexibility.

In three ground-breaking papers published recently in Nature, high-resolution structures of rabbit RyR1 in the closed form were solved independently by three labs using single-particle cryo-EM.[24–26] One of them also solved a putative open-form structure using a buffer of 10 mM Ca.[24] However, previous functional studies have shown that RyR1 features a bell-shaped Ca-response curve[27,28]—it is partially activated by μ*M* Ca, and is in a closed inactivated state at 10 m*M* Ca. Therefore, the physiologically relevant open-form structure of RyR1 is still unknown at high resolution, although it was previously visualized at 10-Å resolution by cryo-EM.[23] The resolutions of these new closed-form structures range from 3.8 Å,[25] 4.8 Å,[26] to 6.1 Å.[24] Together, these studies have offered unprecedented structural insights to the global architecture and conformational variations in the closed state of RyR1.

The structural architecture of RyR1 consists of four identical subunits (see Fig. 1), each containing a large cytoplasmic moiety ($\sim$80% of the total mass) and a trans-membrane domain (TMD). The cytoplasmic moiety is comprised of an N-terminal domain (NTD, divided into three subdomains — NTD_A, NTD_B, and

NTD_C) and a large α-solenoid 1 domain (SOL1) forming the central domains, surrounded by a number of peripheral domains including three SPRY domains (SPRY1, SPRY2, and SPRY3) and two tandems of repeat domains (R12 and R34), and a second α-solenoid domain (SOL2) linking the central and peripheral domains. The N-terminal domain is known to be a hotspot domain for disease mutations.[12] The SOL1 domain harbors key Ca-sensing modules of RyR1, including a CaM-binding domain (CaM-BD2),[10] and a Ca-binding EFH domain containing two EF hand motifs (EFH_N and EFH_C).[29] The three SPRY domains are involved in interaction with other regulatory proteins like FKBP (involving SPRY1 and SPRY2[26]) and Ca_v (involving SPRY2[30,31] and SPRY3[32]). The R12 domain is implicated in coupled gating between neighboring RyR1 molecules which are packed into dense arrays in specialized regions of the SR.[33] The R34 domain, located at the outer corners of RyR1, contains residue S2843 (corresponding to S2808 in RyR2[34]), whose phosphorylation by protein kinase A activates the channel by releasing FKBP12.[35] The SOL2 domain (separated into two parts $SOL2_N$ and $SOL2_C$ by R34) harbors another CaM-binding domain (CaM-BD1) and contains another hotspot domain for disease mutations.[12] There are three divergent regions which vary most between the three RyR isoforms, and are unresolved in the cryo-EM structures.[24] The TMD domain includes six transmembrane helices (S1–S6) reminiscent of the voltage-gated ion channel superfamily. The S6 helices form a channel pore that conducts Ca flow. Remarkably, the TMD of RyR1 has two unique features at the cytoplasmic interface with SOL1 [see Fig. 1(a)], including an extended S6 helix capped by a small C-terminal domain (CTD) and a linker subdomain between S2 and S3 helices (S2S3L) adjacent to the CTD. The strategic locations of these domains make them promising candidates for allosterically transmitting Ca-binding signal from the EFH domain to the channel gate.[24–26] While the static snapshots offered by those new cryo-EM structures provided detailed insights to plausible allosteric pathways that link Ca binding to channel gating, the functional significance of such pathways must be tested by probing the dynamics of RyRs gating under physiological conditions.

Molecular dynamics (MD) simulation is the method of choice for exploring protein dynamics under physiological conditions with atomic resolution.[36] MD has been widely used to study various ion channels,[37–46] including a homology model of the pore-forming transmembrane domain of RyR1.[47] However, MD simulation is computationally very expensive, especially for large protein complexes in explicit solvent. Typical speed of MD simulation on a single computer node equipped with graphics processing unit is 1–10 ns per day for a system of $\sim 10^5$ atoms, although much higher speed can be achieved on a massively parallelized or special-purpose supercomputer.[48] It remains difficult for MD simulation to access microseconds – milliseconds time scales relevant to many functionally important conformational transitions of protein complexes (e.g., the gating of ion channels like RyR1). RyR1 poses a much bigger challenge to MD simulation than other ion channels, because of its enormous size and the incompleteness of the experimentally solve structures (~70% resolved[25]).

To overcome the time-scale limit of MD simulation, coarse-grained modeling has been vigorously pursued using reduced protein representations (e.g., one bead per amino acid residue) and simplified force fields.[49,50] As a popular example of coarse-grained models, the elastic network model (ENM) is constructed by connecting nearby C_α atoms with harmonic springs.[51–53] Despite its simplicity, the normal mode analysis (NMA) of ENM can be used to predict a few low-frequency modes of collective motions, which often compare well with conformational changes observed between experimentally solved protein structures in different functional states[54] (e.g., the gating conformational changes in a pentameric ligand-gated ion channel[55,56] and a tetrameric vanilloid receptor[57]). Numerous studies have established ENM as a useful and efficient means to probe dynamic mechanisms of protein complexes (including membrane proteins[58]) with virtually no limit in timescale or system size (see reviews[59,60]). Unlike MD simulation, ENM-based coarse-grained modeling does not require prior knowledge of all-atom protein structures and is more robust to imperfection in initial structures (such as missing residues and low resolution), therefore it is highly suitable for application to the newly solved cryo-EM structures of RyR1.[24–26] An isotropic version of ENM was previously applied to the N-terminal domain of RyR2 to probe the effect of some disease mutation.[61–63]

To elucidate the allosteric mechanism of RyR1 gating, we have performed a comprehensive coarse-grained modeling based on the cryo-EM structures of the closed form of RyR1.[24–26] First, we used NMA to uncover a key mode of collective motions dominating the observed structural variations in RyR1, which involves large outward/downward movements of several peripheral domains (including domains R12, R34 and $SOL2_N$). Then, we used a perturbation analysis to identify a network of hotspot residues that dictate the above key mode, which coincide well with key functional sites (e.g., the Ca-binding EFH domain) and disease mutations. The above key mode was robustly reproduced by the NMA of the other closed-form structures.[25,26] Finally, we flexibly fitted the closed-form structures of RyR1 into a 10-Å cryo-EM map of the open state,[23] and observed extensive structural changes in the peripheral domains and the central domains, leading to the channel pore opening with outward splaying of S6 helices. This modeling study has offered detailed structural and dynamic insights to the allosteric mechanism of RyRs.

MATERIALS AND METHODS

ENM and NMA

In an ENM, a protein structure is represented as a network of C_α atoms of amino acid residues. Harmonic springs link all pairs of C_α atoms within a cutoff distance R_c chosen to be 25 Å. For RyR1, we used a high R_c to ensure the ENM is adequately connected locally so that the normal modes solved from the ENM (see below) do not have zero eigenvalues (except for six translational and rotational modes). We have verified that the NMA results are not sensitive to the choice of $R_c \geq 25$ Å.

The ENM potential energy is:

$$E=\frac{1}{2}\sum_{i=1}^{N}\sum_{j=1}^{i-1} k_{ij}\theta(R_c-d_{ij,0})(d_{ij}-d_{ij,0})^2 \qquad (1)$$

where N is the number of C_α atoms, $\theta(x)$ is the Heaviside function, d_{ij} is the distance between the C_α atom i and j, $d_{ij,0}$ is the value of d_{ij} as given by a protein structure (e.g., an RyR1 structure with PDB code 4UWA[24]). The spring constant k_{ij} is chosen to be proportional to $d_{ij,0}^{-2}$ for non-bonded interactions (following[64]) and 10 for bonded interactions (in arbitrary unit).

On the basis of the secondary structural assignments from the DSSP program,[65] we partitioned the entire ENM into rigid blocks of α-helices and β-strands together with individual coil residues, and only considered rigid-body rotations and translations of these blocks.[66,67] For 4UWA, such rigid-block partition reduced the dimension from 39888 for the full conformational space to 15764 for the rigid-block subspace. This great reduction in dimension made it possible to perform NMA with modest use of computer memory (~2 GB).

In block NMA,[66,67] the following eigenproblem is solved for the Hessian matrix H which is obtained by calculating the second derivatives of ENM potential energy (see Ref. 68):

$$P^T H P W_m=\lambda_m W_m, \qquad (2)$$

where P is the projection matrix from the rigid-block subspace to the full conformational space, λ_m and W_m represent the eigenvalue and eigenvector of mode m. After excluding six zero modes corresponding to rotations and translations, we kept and numbered non-zero modes starting from 1 in the order of ascending eigenvalue.

For each mode, we used a perturbation analysis to assess how much the eigenvalue changes (represented as $\delta\lambda_m$) in response to a perturbation at a chosen residue position (i.e., by uniformly weakening the springs connected to this position to mimic an Alanine mutation[69–71]). By keeping those residue positions with very high $\delta\lambda_m$ (i.e., ranked in top 1% by $\delta\lambda_m$), we identified a small set of hotspot residues that control the collective motions described by this mode. Our perturbation analysis differs significantly from an alternative energy response calculation (see Ref. 63) — our method is based on the anisotropic ENM and is specific to a particular low-frequency mode that captures the global functional motions (such as mode 2 of RyR1), while the latter method is based on the isotropic Gaussian network model and a few highest-frequency modes that capture the local motions.

To validate ENM-based NMA, we compared each mode (i.e., mode m) with the observed structural change X_{obs} between two superimposed protein structures by calculating an overlap value $I_m=X_{obs}\cdot PW_m/|X_{obs}|$.[72] $|I_m|$ varies between 0 and 1 with higher value meaning greater similarity. I_m^2 gives the fractional contribution of mode m to X_{obs}. The cumulative squared overlap $C_M=\sum_{m=1}^{M} I_m^2$ gives the fractional contribution of the lowest M modes to X_{obs},[72] where $M=20$ or 100. To assess the local flexibility at individual residue positions as described by the lowest M modes, we define the following cummulative flexibility: $\sqrt{\sum_{m=1}^{M}\left(|PW_{m,nx}|^2+|PW_{m,ny}|^2+|PW_{m,nz}|^2\right)}$, where $PW_{m,nx}$, $PW_{m,ny}$, and $PW_{m,nz}$ are the x, y, and z component of mode m's eigenvector at residue n (after being projected to the full conformational space).

To obtain X_{obs} between two RYR1 structures with unknown and missing residues and incompatible residue numbers [e.g., between 4UWA and the other RyR1 structures (PDB code: 3J8E and 3J8H)], we conducted structural alignment to deduce conformational changes between them for the aligned residues. To ensure the robustness of our calculation, we have tried three different structural alignment programs (Mustang-MR Structural Sieving Server,[73] FATCAT pairwise alignment server,[74] MultiProt server[75]).

Validation of hotspot residues in comparison with disease mutations

To validate the functional significance of the predicted hotspot residues, we checked if they overlap with known disease mutations in RyR1 and RyR2 (by calculating the enrichment factor defined as the ratio between the fraction of mutation sites in the selected hotspot residues and that in all cytoplasmic residues). To this end, we collected disease mutations in human RyR1 and RyR2 from the following publicly available online databases (accessed on July 9, 2015):

- ClinVar (http://www.ncbi.nlm.nih.gov/clinvar/): 94 missense mutations in RyR1 and 162 missense mutations in RyR2 whose clinical significance is likely pathogenic or pathogenic;
- The public version of Human Gene Mutation Database (http://www.hgmd.cf.ac.uk/ac/all.php): 312 missense

mutations in RyR1 and 144 missense mutations in RyR2;
- Genetic mutations and inherited arrhythmias database (http://triad.fsm.it/cardmoc/): 134 missense mutations in RyR2.

The RyR1/RyR2 residues involved in the above disease mutations were then mapped to the rabbit RyR1 sequence if they are conserved between human RyR1/RyR2 and rabbit RyR1, resulting in total 407 residue positions identified as mutation sites (ca. 87% of them were resolved in the cryo-EM structures of rabbit RyR1).

Flexible fitting of cryo-EM map

Previously we developed a coarse-grained method based on a modified form of ENM to flexibly fit a given Cα-only structure in an initial state into the cryo-EM density map of an end state (available at http://enm.lobos.nih.gov/emff/start_emff.html). It allows us to model the conformational changes from the initial state to the end state at amino-acid level of details.[76] The initial structure was rigidly fitted into the cryo-EM map using the colores command of the SITUS program (http://situs.biomachina.org/). Then we ran flexible fitting to iteratively generate a series of up to 10 conformations with increasing root mean squared deviation (RMSD) from the initial structure and gradually improving fitting to the given cryo-EM map as assessed by the cross correlation coefficient (CCC) with the cryo-EM densities.[76] The flexible fitting was terminated upon saturation of CCC.

RESULTS AND DISCUSSION

NMA predicts key collective motions and hotspot residues involved in the RyR1 gating transition

We have performed ENM-based NMA and perturbation analysis on three closed-form structures solved by cryo-EM.[24–26] We will focus on the closed-form structure from Ref.,[24] and similar results were obtained for the other two structures.

NMA results for the closed-form structures of RyR1

Starting from the closed-form structure of RyR1 (PDB code: 4UWA), we constructed a C_α-only ENM by linking each pair of residues within 25 Å by a harmonic spring with a distance-dependent force constant (see Methods). Then we performed block NMA[66,67] (see Methods) to obtain a spectrum of total 12,688 modes. Here we focused on the lowest 20 modes, each describing a specific pattern of collective motion energetically favored by the given structure (for results of the lowest 100 modes, see Table S1 and Fig. S1 in Supporting Information).

For validation of these modes, we assessed how well they capture the experimentally observed conformational changes from 4UWA to three different closed-state conformations of RyR1 constructed from the heterogeneous cryo-EM data set (named C1, C2, C3[24]). To this end, we calculated the overlap between each mode and the observed conformational change and the cumulative squared overlap of the lowest 20 modes (see Methods). For C1 and C2, >50% of the observed conformational change (with RMSD of 3.2 Å and 2.6 Å, respectively) is captured by the lowest 20 modes with the maximal overlap 0.63 and 0.57 at mode 2 (see Supporting Information Table S1). For C3, the observed conformational change is much smaller (with RMSD of 1.6 Å), and involves primarily high-frequency modes beyond the lowest 20 or 100 (see Supporting Information Table S1). The above finding agrees with Ref.[24] which found one major motional mode by comparing C1, C2, and C3. Our mode 2 shares similar features to the mode described in Ref.[24]—large rocking movements of the peripheral domains and no dilation of the gate. The same calculation was done for the conformational change from 4UWA to the putative open-form structure (PDB code: 4UWE) in Ref.[24] which is more likely to be an alternative closed-form conformation. It was found the lowest 20 modes captured 55% of the observed conformational change, with mode 2 dominating with the highest overlap 0.69 [see Fig. 2(a)]. Therefore, the large structural fluctuations in the closed state involve a dominant mode (mode 2) with other low-frequency modes contributing to a lesser extent [see Fig. 2(a)].

To assess the differences between the three closed-form structures solved by three labs,[24–26] we compared the lowest 20 modes with the observed structural differences between 4UWA and the other two closed-form structures (PDB code: 3J8E and 3J8H). Although only 40–60% residues can be structurally aligned between them, we were able to calculate the overlap for each mode (and cumulative squared overlap for the lowest 20 or 100 modes, see Supporting Information Table S1) involving the aligned residues. More than 44% of the structural difference between 4UWA and 3J8E is captured by the lowest 20 modes (with maximal overlap >0.56 at mode 2). More than 58% of the difference between 4UWA and 3J8H is captured by the lowest 100 modes although the lowest 20 modes are inadequate. The above results are robust to the choice of different structural alignment methods (see Supporting Information Table S1). Therefore, a large part of the structural differences between the three closed-form structures can be attributed to conformational heterogeneity of the closed state involving primarily the lowest 20 or 100 modes, although modeling imperfections like missing residues and different domain assignments may also contribute.

Then we visualized the collective motions predicted by mode 2 [see Fig. 3(a)]. Similar to the domain motions

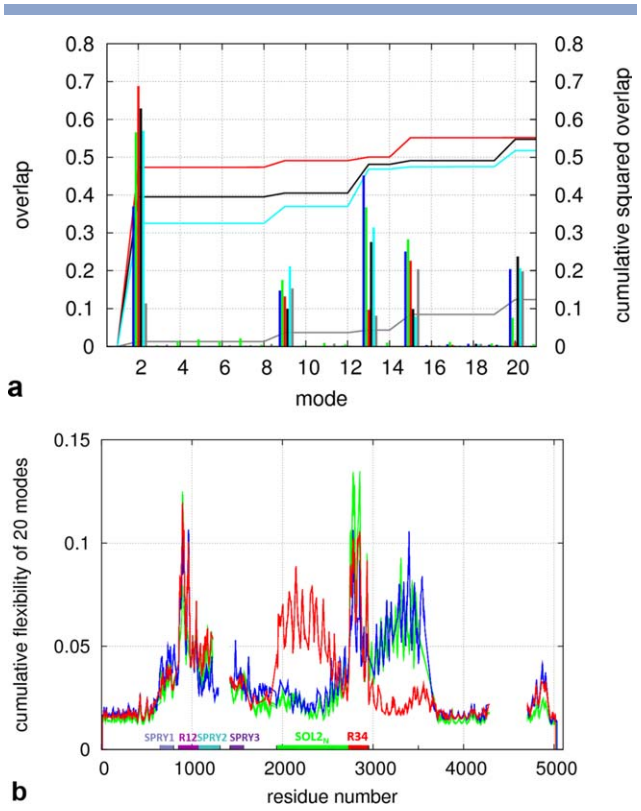

Figure 2

Results of NMA for the lowest 20 modes calculated from the closed-form structure of RyR1 (PDB code: 4UWA): (**a**) the overlap and cumulative squared overlap as a function of mode number (shown as impulses and lines, respectively) for the observed conformational changes to the putative open-form structure (PDB code: 4UWE, red), two other closed-form structures (PDB code: 3J8E, green; 3J8H, blue), and three different closed-state structures (C1, black; C2, cyan; C3, gray). (**b**) The cumulative flexibility of lowest 20 modes as a function of residue number for the following three closed-form structures: 4UWA (red), 3J8E (green), and 3J8H (blue). The domains with high flexibility are marked by horizontal bars colored as follows: SPRY1 (ice blue), R12 (purple), SPRY2 (cyan), SPRY3 (violet), $SOL2_N$ (green), and R34 (red). Note the broad peak at $SOL2_N$ was shifted rightward in 3J8E and 3J8H due to a swap of $SOL2_N$ and $SOL2_C$ in domain assignment.

observed by a cryo-EM study of RyR1 in both closed and open state,[23] mode 2 predicts large downward and outward motions of the peripheral domains (including domains R12, R34, and $SOL2_N$) accompanied by small upward motions of the central domains (including domains NTD and SOL1) while the TMD remains essentially unchanged [e.g., no gate opening, see Fig. 3(a)]. Therefore, as found in many large protein complexes[52,54] including ion channels,[55–57] the ENM-based NMA offers qualitatively good description of the functional conformational changes involved in RyR1 gating (see below for a quantitative analysis of the contribution of mode 2 to RyR1 gating transition as modeled by cryo-EM flexible fitting).

To test the robustness of the key mode deduced from the NMA of 4UWA, we performed NMA for the other two closed-form structures solved independently (PDB codes: 3J8E and 3J8H). Encouragingly, for both structures, mode 2 predicts similar collective motions to mode 2 of 4UWA with large downward and outward motions of the peripheral domains (including domains R12, R34, and $SOL2_N$) and the TMD unchanged [see Fig. 3(b,c)].

Analysis of hotspot residues that control the key mode

After establishing the dynamic importance of mode 2, we used an ENM-based perturbation analysis (see Methods) to identify a network of hotspot residues that control the inter-domain motions described by this mode (see Fig. 3). To this end, we calculated for each residue position a score $\delta\lambda_m$ [see Supporting Information Fig. S2(a)] which assesses how much the eigenvalue of mode 2 changes in response to a perturbation at the given residue position.[69–71] Then we kept those hotspot residue positions ranked in top 0.5–10% by $\delta\lambda_m$, which are predicted to control the collective motions described by this mode. To validate the functional importance of the predicted hotspot residues, we quantitatively assess how well the predicted hotspot residues overlap with the known disease mutations in RyR1 and RyR2 collected from online databases (see Methods). To this end, we calculated an enrichment factor (see Methods) to measure enrichment of disease mutations in the selected hotspot residues. Encouragingly, the enrichment factor increases from ~1 to 3.3 as the cutoff percentile decreases from 10% to 0.5% and ascends sharply near 1% [see Supporting Information Fig. S2(b)], suggesting a good overlap between the hotspot residues (e.g., selected in top 1% by $\delta\lambda_m$) and the disease mutation sites, thus supporting the functional importance of the hotspot residues. Notably, the positive enrichment result was only obtained for 3J8H but not for 4UWA or 3J8E [see Supporting Information Fig. S2(b)], which can be attributed to discrepancies in the assignments of residues/domains in those cryo-EM structures (e.g., swap of $SOL2_N$ and $SOL2_C$ in 4UWA compared with 3J8E and 3J8H, different assignments of three SPRY domains, etc). Thanks to higher resolution of 3J8H, it most likely gave more accurate assignments, therefore better correlation between hotspot residue positions and mutation sites.

On the basis of the above enrichment analysis, we focused on the following top 1% hotspot residues in 3J8H [see Fig. 3(c)]:

Residues Y2849 and G1507 are at the interface between R34 and SPRY3 of an adjacent subunit, which are near the phosphorylation site S2843 (S2843 is on a disordered loop and not included in our modeling). This finding suggests that phosphorylation may modulate the

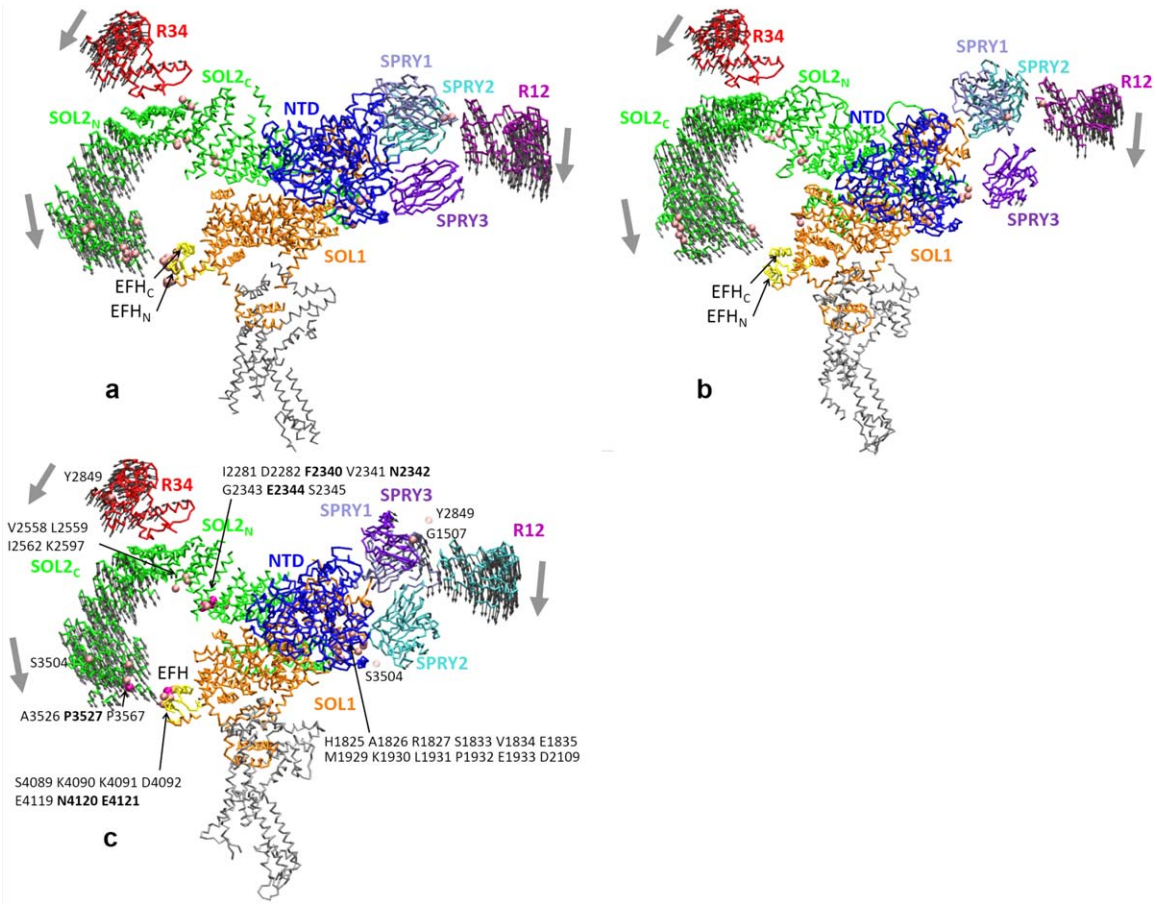

Figure 3

Collective motions and hotspot residues predicted by mode 2 calculated from the following closed-form structures of RyR1: (**a**) 4UWA, (**b**) 3J8E, and (**c**) 3J8H: The various domains are colored with the same color scheme as Figure 1. Large movements of domains R12, R34, and $SOL2_N$ are depicted as vector field and bold arrows, which are very similar between the three structures. Hotspot residues are shown as pink spheres. In panel (c), the residue numbers of hotspot residues are labeled, and the mutation sites are shown as magenta spheres (labeled in bold font).

collective motions of mode 2 by perturbing the hotspot residues at the R34-SPRY3 interface.

Residues H1825, A1826, R1827, S1833, V1834, E1835, M1929, K1930, L1931, P1932, E1933, and D2109 are at the SOL1-SOL2 interface, which are in proximity to another hotpot residue S3504 from $SOL2_C$ of an adjacent subunit. Notably, residues 1837–2168 are implicated in coupling to Ca_v.[77] So binding with Ca_v may modulate the collective motions of mode 2 by perturbing the hotspot residue at the SOL1-SOL2 interface.

Residues I2281, D2282, F2340, V2341, N2342, G2343, E2344, S2345, V2558, L2559, I2562, and K2597 are located at the central hinge of the curved SOL2 domain, which include three disease mutation sites (F2340, N2342, and E2344). These residues may control the outward and downward movement of SOL2 [see Fig. 3(c)].

At the tip of the curved SOL2 domain, residues A3526, P3527, and P3567 are within a minimal distance of ~19 Å from residues S4089, K4090, K4091, D4092, E4119, N4120, and E4121 of the EFH domain of SOL1, including three disease mutation sites (P3527, N4120, and E4121). Note the SOL2–EFH distance could be even smaller if the disordered residues at the tip of SOL2 are taken into account. The SOL2-EFH interactions may directly couple the large downward motion of SOL2 to EFH's smaller changes associated with Ca binding. This coupling may enable Ca binding to modulate the collective motions of mode 2 underlying the gating transition of RyR1.

In sum, the network of hotspot residues that control mode 2 overlap well with key functional sites (involved in phosphorylation and binding with Ca_v and Ca) and disease mutations, supporting the functional relevance of the collective motions described by this mode. The involvement of global collective motions in RyR1 gating can naturally account for allosteric couplings between distant functional domains in RyR1, which may underscore the observed synergistic effects of domain unzipping between NTD and SOL2,[78] hyper-posphorylation at S2843 of R34,[79] and FKBP dissociation.[78,79]

Analysis of differences between the three closed-form structures

Despite overall similarity, we found some interesting differences in the distribution of hotspot residues between the three closed-form structures (see Fig. 3):

In 3J8E, there are no top 1% hotspot residues in the EFH domain, suggesting a weaker coupling at the SOL2-EFH interface than in 4UWA. This is consistent with the analysis of structural differences between 3J8E and 4UWA (see Supporting Information Table S1), which found that 3J8E is more closed-form-like than 4UWA when projected along mode 2 [with the SOL2 in a more upward position and further from the EFH, see Fig. 3(b)].

In 3J8H, there are fewer hotspot residues in the EFH domain than in 4UWA, suggesting a weaker coupling at the SOL2-EFH interface than in 4UWA (but still stronger than in 3J8E). This is consistent with the analysis of structural differences between 3J8H, 3J8E, and 4UWA (see Supporting Information Table S1) which found that 3J8H is intermediate between 3J8E and 4UWA when projected along mode 2.

What causes the above structural differences between 4UWA, 3J8H, and 3J8E? There is evidence for differences in FKBP binding between these structures. While FKBP had low occupancy and was not modeled in 4UWA, it was well resolved in both 3J8E and 3J8H. Notably, 3J8E was solved for dephosphorylated RyR1[26] which favors FKBP binding.[79] A FKBP-binding helix (residues 2135–2155) was resolved in 3J8E, and a corresponding structural element (a β-strand) was also resolved in 3J8H. But no corresponding structural element was present in 4UWA. Therefore, stronger binding of FKBP in 3J8E and 3J8H may result in a more closed-form-like structure than 4UWA. Consequently, FKBP binding can inhibit the RyR1 channel[80] in two ways: first, it damps the collective motions of mode 2 by binding to the hinge region; second, it structurally displaces RyR1 further away from the open-state conformation along mode 2. Indeed, a cryo-EM study found conformational changes in RyR2 induced by FKBP12.6 binding,[81] featuring upward movements of the peripheral domains when FKBP12 is present,[2] which is opposite to the downward movements observed in the closed-to-open transition.

Flexibility analysis based on NMA

To assess the total contributions of all lowest 20 modes to the local flexibility of RyR1 in the closed state, we calculated the cumulative flexibility (see Methods) as a function of residue number [see Fig. 2(b), also see Supporting Information Fig. S1 for the results of the lowest 100 modes]. Similar to mode 2, the highest flexibility was found in domains R12, R34, and $SOL2_N$, followed by moderately high flexibility in the SPRY domains, and low flexibility in the central domains and TMD [see Fig. 2(b)]. Consistent with our finding, cryo-EM data indicated that the peripheral domains are more flexible and less well-resolved than the central domains and TMD.[24–26] The robustness of our flexibility analysis is supported by the good agreement between three different closed-state structures [see Fig. 2(b)] (except for a swap of $SOL2_N$ and $SOL2_C$ between 4UWA and the other two, and different assignments of three SPRY domains between 3J8H and the other two). We also calculated the flexibility profiles for each of the lowest 20 modes (see Supporting Information Fig. S5), which exhibit similar features to the cumulative flexibility.

Flexible fitting of cryo-EM data reveals detailed structural changes during the RyR1 closed-to-open transition

The NMA in the closed state has revealed key collective motions as described by mode 2, which resemble key structural changes between the closed and open state as observed by cryo-EM at 10-Å resolution.[23] To ultimately determine the structural and dynamic basis of RyR1 gating, it is critical to visualize the open state and the closed-to-open transition with structural details. Despite higher resolution (8.5 Å), the putative open-state cryo-EM structure (PDB id: 4UWE) was solved under a Ca concentration which is known to favor a closed inactive state of RyR1. To model the open-state conformation of RyR1 at high resolution, we used a modified ENM[76] to flexibly fit a closed-state structure of RyR1 into the 10-Å cryo-EM density map of RyR1 in the open state.[23] Among various cryo-EM flexible fitting methods, our method[76] is more efficient and tolerant of structural imperfections than those all-atom flexible fitting methods,[82,83] making it highly applicable to large incomplete protein structures like those of RyR1 solved by cryo-EM. To model the closed-to-open conformational changes of RyR1 at amino-acid level of details, we generated a series Cα-only models which deviate progressively (with increasing RMSD) from the initial structure, and fit the open-state cryo-EM map with gradually higher CCC [see Supporting Information Fig. S3(a), movie S1 and S2]. We then projected the cryo-EM-fitted conformational changes along mode 2 solved for the closed-state structure (see above) to assess its involvement in the closed-to-open transition of RyR1.

Starting from 3J8H (the highest-resolution closed-state structure among 4UWA, 3J8E, and 3J8H), our flexible fitting yielded an open-state RyR1 model with CCC improved from 0.65 to 0.85 and RMSD ~6 Å relative to 3J8H [see Supporting Information Fig. S3(a) and Fig. 4(a)]. The cryo-EM-fitted closed-to-open conformational changes feature large outward and downward movements of the peripheral domains [including R12, R34, SPRY domains, and $SOL2_C$, see Fig. 4(b)], opening of the inter-subunit interfaces in the NTD ring[84] [see Fig.

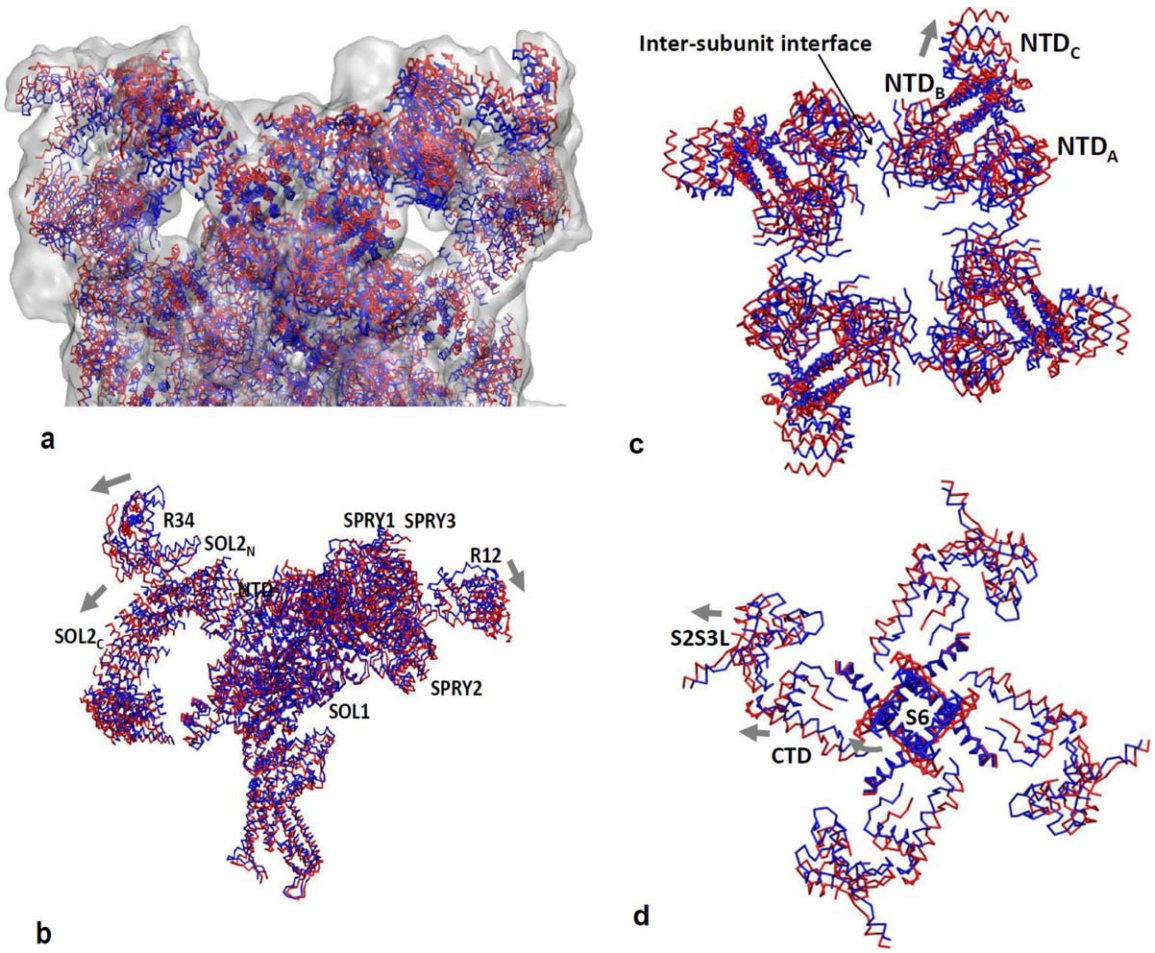

Figure 4

Results of the cryo-EM flexible fitting of RyR1 starting from 3J8H: (**a**) Top view of the RyR1 structures fitted into the 10-Å cryo-EM map of RyR1 in the open state; (**b**) Side view of the RyR1 structures with a representative subunit shown; (**c**) Top view of the NTD rings of RyR1 structures; (**d**) Top view of the TMD of RyR1 structures with only the S2S3L, S6 helices, and CTD shown. The initial closed-form structure (3J8H) is colored in blue and the fitted open-form structure is colored in red. Domain movements are marked by arrows.

4(c)], outward movement of the S2S3L domain and CTD [see Fig. 4(d)], and opening of the channel pore via outward splaying of S6 helices [see Fig. 4(d)]. Remarkably, we clearly observed a more open channel pore (with a diameter ~13 Å near G4934) than the closed structure 3J8H (with a diameter ~10 Å near G4934), which is wider than the putative open-form structure 4UWE (with a diameter ~11 Å near G4934) and comparable to the diameter of an open-channel structure of TRPV1 (PDB code: 3J5Q) near G683. These structural observations substantiate, with amino-acid level of details, the earlier observations of closed-to-open conformational changes in RyR1 by cryo-EM at low resolution.[23] Our finding supports an allosteric mechanism whereby the outward/downward moving peripheral domains trigger dilation of the NTD ring and the channel pore by pulling outward intermediate domains like S2S3L and CTD.

The cryo-EM-fitted closed-to-open conformational changes initially involve mode 2 (with initial overlap = 0.56), whose contribution gradually declines toward the open state (with final overlap = 0.33) [see Supporting Information Fig. S3(b)]. This finding supports the importance of mode 2 to the initiation of the closed-to-open transition in RyR1. Because mode 2 does not involve channel opening in the TMD, other modes must be recruited later during the transition to enable channel opening. Our finding implies the existence of an intermediate during the gating transition with the cytosolic domains activated (via mode 2) while the channel remains closed, pointing to a "loose coupling" between the cytosolic domains and the channel gate in RyR1 gating.

The above finding of multiple modes involved in the closed-to-open conformational transition in RyR1 suggests that these functional motions are inherently

anharmonic and not fully described by a harmonic model like ENM. Indeed, the opening of RyR1 channel necessitates the breaking of many inter-domain/subunit interactions not favored by elastic interactions in ENM. Therefore, it is appropriate to model such conformational changes using a modified anharmonic form of ENM[76] that allows breaking of residue contacts at finite cost of energy. This approach will be generally applicable to the modeling of closed-to-open transitions in various other ion channels.

To verify the robustness of the flexible fitting results, we also ran it starting from alternative closed-state structures 4UWA and 3J8E, which yielded similar closed-to-open conformational changes (see Supporting Information Fig. S4) with mode 2 involved [see Supporting Information Fig. S3(b)].

CONCLUSION

In conclusion, to elucidate the allosteric mechanism of RyR1, we performed a comprehensive coarse-grained modeling based on the newly solved cryo-EM structures of RyR1 in the closed state. Our coarse-grained NMA has captured a key mode of collective motions dominating the observed structural variations in RyR1, which features large outward and downward movements of the peripheral domains (including R12, R34, and $SOL2_N$) with little changes in the TMD domain, and involves a network of hotspot residues at inter-domain hinge regions that coincide with key functional sites (e.g., binding sites for Ca_v and Ca) and disease mutations. In particular, we found a key interaction between hotspot residues of the SOL2 domain and the EFH domain, which allows for direct coupling of Ca binding to the collective motions as captured by this mode. Our flexible fitting of a cryo-EM map in the open state has predicted extensive structural changes involving the peripheral domains (e.g., R12 and R34) and the central domains (e.g., NTD), leading to the channel opening via outward splaying of S6 helices. This study is, to our knowledge, the first dynamic modeling study of the entire RyR1 after the publication of the new RyR1 structures.[24–26] Our findings have offered new structural and dynamic insights to the allosteric mechanism of RyRs via modulation of the key collective motions involved in channel gating. The predicted hotspot residues [see Fig. 3(c)] and open-state conformation (see Supporting Information for the coordinates file) of RyR1 will offer useful guidance for future mutational and functional studies. For example, site specific mutations or crosslinking experiments that target the SOL2-EFH interactions are predicted to strongly affect the RyR1 gating function.

Note: the role of EFH in directly sensing Ca binding and triggering channel gating was cast in doubt by a recent study showing its deletion did not compromise Ca activation of RyR1 (unpublished result from the lab of Chen SR). It remains possible that EFH plays a Ca-dependent regulatory role in RyR1 gating.

ACKNOWLEDGMENT

Computational support was provided by the Center for Computational Research at the University at Buffalo. The author thanks Dr. Efremov for sharing the coordinate files for the closed-state models C1-C3 and open-state models O1-O4. The author also thanks Dr. Filip Van Petegem for valuable comments on this work.

REFERENCES

1. Van Petegem F. Ryanodine receptors: structure and function. J Biol Chem 2012;287:31624–31632.
2. Van Petegem F. Ryanodine receptors: allosteric ion channel giants. J Mol Biol 2015;427:31–53.
3. Ikemoto N, Yamamoto T. Regulation of calcium release by interdomain interaction within ryanodine receptors. Front Biosci J Vir Lib 2002;7:d671–d683.
4. Chen SR, Zhang L, MacLennan DH. Characterization of a Ca2+ binding and regulatory site in the Ca2+ release channel (ryanodine receptor) of rabbit skeletal muscle sarcoplasmic reticulum. J Biol Chem 1992;267:23318–23326.
5. Chen SR, Zhang L, MacLennan DH. Antibodies as probes for Ca2+ activation sites in the Ca2+ release channel (ryanodine receptor) of rabbit skeletal muscle sarcoplasmic reticulum. J Biol Chem 1993; 268:13414–13421.
6. Fessenden JD, Feng W, Pessah IN, Allen PD. Mutational analysis of putative calcium binding motifs within the skeletal ryanodine receptor isoform, RyR1. J Biol Chem 2004;79:53028–53035.
7. Hayek SM, Zhu X, Bhat MB, Zhao J, Takeshima H, Valdivia HH, Ma J. Characterization of a calcium-regulation domain of the skeletal-muscle ryanodine receptor. Biochem J 2000;351:57–65.
8. Treves S, Chiozzi P, Zorzato F. Identification of the domain recognized by anti-(ryanodine receptor) antibodies which affect Ca(2+)-induced Ca2+ release. Biochem J 1993;291:757–763.
9. Brillantes AB, Ondrias K, Scott A, Kobrinsky E, Ondriasova E, Moschella MC, Jayaraman T, Landers M, Ehrlich BE, Marks AR. Stabilization of calcium release channel (ryanodine receptor) function by FK506-binding protein. Cell 1994;77:513–523.
10. Lau K, Chan MM, Van Petegem F. Lobe-specific calmodulin binding to different ryanodine receptor isoforms. Biochemistry 2014;53:932–946.
11. Hwang JH, Zorzato F, Clarke NF, Treves S. Mapping domains and mutations on the skeletal muscle ryanodine receptor channel. Trends Mol Med 2012;18:644–657.
12. Betzenhauser MJ, Marks AR. Ryanodine receptor channelopathies. Pflugers Arch Eur J Physiol 2010;460:467–480.
13. ushnir A, Marks AR. The ryanodine receptor in cardiac physiology and disease. Adv Pharmacol 2010;59:1–30.
14. Lanner JT. Ryanodine receptor physiology and its role in disease. Adv Exp Med Biol 2012;740:217–234.
15. Dulhunty AF, Casarotto MG, Beard NA. The ryanodine receptor: a pivotal Ca2+ regulatory protein and potential therapeutic drug target. Curr Drug Targets 2011;12:709–723.
16. Amador FJ, Stathopulos PB, Enomoto M, Ikura M. Ryanodine receptor calcium release channels: lessons from structure-function studies. FEBS J 2013;280:5456–5470.
17. Radermacher M, Wagenknecht T, Grassucci R, Frank J, Inui M, Chadwick C, Fleischer S. Cryo-EM of the native structure of the calcium release channel/ryanodine receptor from sarcoplasmic reticulum. Biophys J 1992;61:936–940.

18. Radermacher M, Rao V, Grassucci R, Frank J, Timerman AP, Fleischer S, Wagenknecht T. Cryo-electron microscopy and three-dimensional reconstruction of the calcium release channel/ryanodine receptor from skeletal muscle. J Cell Biol 1994;127:411–423.
19. Ludtke SJ, Serysheva II, Hamilton SL, Chiu W. The pore structure of the closed RyR1 channel. Structure 2005;13:1203–1211.
20. Samso M, Wagenknecht T, Allen PD. Internal structure and visualization of transmembrane domains of the RyR1 calcium release channel by cryo-EM. Nat Struct Mol Biol 2005;12:539–544.
21. Serysheva II, Hamilton SL, Chiu W, Ludtke SJ. Structure of Ca2+ release channel at 14 A resolution. J Mol Biol 2005;345:427–431.
22. Serysheva II, Ludtke SJ, Baker ML, Cong Y, Topf M, Eramian D, Sali A, Hamilton SL, Chiu W. Subnanometer-resolution electron cryomicroscopy-based domain models for the cytoplasmic region of skeletal muscle RyR channel. Proc Natl Acad Sci USA 2008;105: 9610–9615.
23. Samso M, Feng W, Pessah IN, Allen PD. Coordinated movement of cytoplasmic and transmembrane domains of RyR1 upon gating. PLoS Biol 2009;7:e85.
24. Efremov RG, Leitner A, Aebersold R, Raunser S. Architecture and conformational switch mechanism of the ryanodine receptor. Nature 2015;517:39–43.
25. Yan Z, Bai XC, Yan C, Wu J, Li Z, Xie T, Peng W, Yin CC, Li X, Scheres SH, Shi Y, Yan N. Structure of the rabbit ryanodine receptor RyR1 at near-atomic resolution. Nature 2015;517:50–55.
26. Zalk R, Clarke OB, des Georges A, Grassucci RA, Reiken S, Mancia F, Hendrickson WA, Frank J, Marks AR. Structure of a mammalian ryanodine receptor. Nature 2015;517:44–49.
27. Smith JS, Coronado R, Meissner G. Single channel measurements of the calcium release channel from skeletal muscle sarcoplasmic reticulum. Activation by Ca2+ and ATP and modulation by Mg2+. J Gen Physiol 1986;88:573–588.
28. Bezprozvanny I, Watras J, Ehrlich BE. Bell-shaped calcium-response curves of Ins(1,4,5)P3- and calcium-gated channels from endoplasmic reticulum of cerebellum. Nature 1991;351:751–754.
29. Xiong H, Feng X, Gao L, Xu L, Pasek DA, Seok JH, Meissner G. Identification of a two EF-hand Ca2+ binding domain in lobster skeletal muscle ryanodine receptor/Ca2+ release channel. Biochemistry 1998;37:4804–4814.
30. Tae H, Casarotto MG, Dulhunty AF. Ubiquitous SPRY domains and their role in the skeletal type ryanodine receptor. Eur Biophys J 2009;39:51–59.
31. Leong P, MacLennan DH. A 37-amino acid sequence in the skeletal muscle ryanodine receptor interacts with the cytoplasmic loop between domains II and III in the skeletal muscle dihydropyridine receptor. J Biol Chem 1998;273:7791–7794.
32. Sheridan DC, Takekura H, Franzini-Armstrong C, Beam KG, Allen PD, Perez CF. Bidirectional signaling between calcium channels of skeletal muscle requires multiple direct and indirect interactions. Proc Natl Acad Sci USA 2006;103:19760–19765.
33. Marx SO, Ondrias K, Marks AR. Coupled gating between individual skeletal muscle Ca2+ release channels (ryanodine receptors). Science 1998;281:818–821.
34. Wehrens XH, Lehnart SE, Reiken S, Vest JA, Wronska A, Marks AR. Ryanodine receptor/calcium release channel PKA phosphorylation: a critical mediator of heart failure progression. Proc Natl Acad Sci USA 2006;103:511–518.
35. Reiken S, Lacampagne A, Zhou H, Kherani A, Lehnart SE, Ward C, Huang F, Gaburjakova M, Gaburjakova J, Rosemblit N, Warren MS, He KL, Yi GH, Wang J, Burkhoff D, Vassort G, Marks AR. PKA phosphorylation activates the calcium release channel (ryanodine receptor) in skeletal muscle: defective regulation in heart failure. J Cell Biol 2003;160:919–928.
36. Karplus M, McCammon JA. Molecular dynamics simulations of biomolecules. Nat Struct Biol 2002;9:646–652.
37. Nury H, Poitevin F, Van Renterghem C, Changeux JP, Corringer PJ, Delarue M, Baaden M. One-microsecond molecular dynamics simulation of channel gating in a nicotinic receptor homologue. Proc Natl Acad Sci USA 2010;107:6275–6280.
38. Zhu F, Hummer G. Pore opening and closing of a pentameric ligand-gated ion channel. Proc Natl Acad Sci USA 2010;107:19814–19819.
39. Nury H, Van Renterghem C, Weng Y, Tran A, Baaden M, Dufresne V, Changeux JP, Sonner JM, Delarue M, Corringer PJ. X-ray structures of general anaesthetics bound to a pentameric ligand-gated ion channel. Nature 2011;469:428–431.
40. Calimet N, Simoes M, Changeux JP, Karplus M, Taly A, Cecchini M. A gating mechanism of pentameric ligand-gated ion channels. Proc Natl Acad Sci USA 2013;110:E3987–3996.
41. Vargas E, Yarov-Yarovoy V, Khalili-Araghi F, Catterall WA, Klein ML, Tarek M, Lindahl E, Schulten K, Perozo E, Bezanilla F, Roux B. An emerging consensus on voltage-dependent gating from computational modeling and molecular dynamics simulations. J Gen Physiol 2012;140:587–594.
42. Delemotte L, Klein ML, Tarek M. Molecular dynamics simulations of voltage-gated cation channels: insights on voltage-sensor domain function and modulation. Front Pharmacol 2012;3:97.
43. Lindahl E, Sansom MS. Membrane proteins: molecular dynamics simulations. Curr Opin Struct Biol 2008;18:425–431.
44. Dong H, Zhou HX. Atomistic mechanism for the activation and desensitization of an AMPA-subtype glutamate receptor. Nat Commun 2011;2:354
45. Du J, Dong H, Zhou HX. Gating mechanism of a P2X4 receptor developed from normal mode analysis and molecular dynamics simulations. Proc Natl Acad Sci USA 2012;109:4140–4145.
46. Jensen MO, Jogini V, Borhani DW, Leffler AE, Dror RO, Shaw DE. Mechanism of voltage gating in potassium channels. Science 2012; 336:229–233.
47. Shirvanyants D, Ramachandran S, Mei Y, Xu L, Meissner G, Dokholyan NV. Pore dynamics and conductance of RyR1 transmembrane domain. Biophys J 2014;106:2375–2384.
48. Klepeis JL, Lindorff-Larsen K, Dror RO, Shaw DE. Long-timescale molecular dynamics simulations of protein structure and function. Curr Opin Struct Biol 2009;19:120–127.
49. Tozzini V. Coarse-grained models for proteins. Curr Opin Struct Biol 2005;15:144–150.
50. Tozzini V. Minimalist models for proteins: a comparative analysis. Q Rev Biophys 2010;43:333–371.
51. Atilgan AR, Durell SR, Jernigan RL, Demirel MC, Keskin O, Bahar I. Anisotropy of fluctuation dynamics of proteins with an elastic network model. Biophys J 2001;80:505–515.
52. Tama F, Sanejouand YH. Conformational change of proteins arising from normal mode calculations. Protein Eng 2001;14:1–6.
53. Zheng W, Doniach S. A comparative study of motor-protein motions by using a simple elastic-network model. Proc Natl Acad Sci USA 2003;100:13253–13258.
54. Krebs WG, Alexandrov V, Wilson CA, Echols N, Yu H, Gerstein M. Normal mode analysis of macromolecular motions in a database framework: developing mode concentration as a useful classifying statistic. Proteins 2002;48:682–695.
55. Sauguet L, Shahsavar A, Poitevin F, Huon C, Menny A, Nemecz A, Haouz A, Changeux JP, Corringer PJ, Delarue M. Crystal structures of a pentameric ligand-gated ion channel provide a mechanism for activation. Proce Natl Acad Sci USA 2014;111:966–971.
56. Taly A, Delarue M, Grutter T, Nilges M, Le Novere N, Corringer PJ, Changeux JP. Normal mode analysis suggests a quaternary twist model for the nicotinic receptor gating mechanism. Biophys J 2005; 88:3954–3965.
57. Zheng W, Qin F. A combined coarse-grained and all-atom simulation of TRPV1 channel gating and heat activation. J Gen Physiol, in press.
58. Bahar I, Lezon TR, Bakan A, Shrivastava IH. Normal mode analysis of biomolecular structures: functional mechanisms of membrane proteins. Chem Rev 2010;110:1463–1497.

59. Bahar I, Rader AJ. Coarse-grained normal mode analysis in structural biology. Curr Opin Struct Biol 2005;15:586–592.
60. Tama F, Brooks CL. Symmetry, form, and shape: guiding principles for robustness in macromolecular machines. Annu Rev Biophys Biomol Struct 2006;35:115–133.
61. Walpoth BN, Erman B. Regulation of ryanodine receptor RyR2 by protein–protein interactions: prediction of a PKA binding site on the N-terminal domain of RyR2 and its relation to disease causing mutations. F1000Research 2015;4:29.
62. Erman B, Walpoth N. The disease mutation A77V in Ryanodine receptor RyR2 induces changes in energy conduction pathways in the protein. Nat Proc Available at: <http://hdlhandlenet/10101/npre201166781> 2011.
63. Walpoth NB, Erman B. The effect of point mutations on energy conduction pathways in proteins. 2011;arXiv:11115165.
64. Yang L, Song G, Jernigan RL. Protein elastic network models and the ranges of cooperativity. Proc Natl Acad Sci USA 2009;106:12347–12352.
65. Kabsch W, Sander C. Dictionary of protein secondary structure: pattern recognition of hydrogen-bonded and geometrical features. Biopolymers 1983;22:2577–2637.
66. Tama F, Gadea FX, Marques O, Sanejouand YH. Building-block approach for determining low-frequency normal modes of macromolecules. Proteins 2000;41:1–7.
67. Li G, Cui Q. Analysis of functional motions in Brownian molecular machines with an efficient block normal mode approach: myosin-II and Ca2+ -ATPase. Biophys J 2004;86:743–763.
68. Zheng W, Auerbach A. Decrypting the sequence of structural events during the gating transition of pentameric ligand-gated ion channels based on an interpolated elastic network model. PLoS Comput Biol 2011;7:e1001046.
69. Zheng W, Brooks BR, Doniach S, Thirumalai D. Network of dynamically important residues in the open/closed transition in polymerases is strongly conserved. Structure 2005;13:565–577.
70. Zheng W, Brooks BR, Thirumalai D. Low-frequency normal modes that describe allosteric transitions in biological nanomachines are robust to sequence variations. Proc Natl Acad Sci USA 2006;103:7664–7669.
71. Zheng W, Tekpinar M. Large-scale evaluation of dynamically important residues in proteins predicted by the perturbation analysis of a coarse-grained elastic model. BMC Struct Biol 2009;9:45.
72. Zheng W. Coarse-grained modeling of the structural states and transition underlying the powerstroke of dynein motor domain. J Chem Phys 2012;136:155103.
73. Konagurthu AS, Reboul CF, Schmidberger JW, Irving JA, Lesk AM, Stuckey PJ, Whisstock JC, Buckle AM. MUSTANG-MR structural sieving server: applications in protein structural analysis and crystallography. PloS One 2010;5:e10048.
74. Ye Y, Godzik A. Flexible structure alignment by chaining aligned fragment pairs allowing twists. Bioinformatics 2003;19 (Suppl 2):ii246–ii255.
75. Shatsky M, Nussinov R, Wolfson HJ. A method for simultaneous alignment of multiple protein structures. Proteins 2004;56:143–156.
76. Zheng W. Accurate flexible fitting of high-resolution protein structures into cryo-electron microscopy maps using coarse-grained pseudo-energy minimization. Biophys J 2011;100:478–488.
77. Proenza C, O'Brien J, Nakai J, Mukherjee S, Allen PD, Beam KG. Identification of a region of RyR1 that participates in allosteric coupling with the alpha(1S) (Ca(V)1.1) II-III loop. J Biol Chem 2002;277:6530–6535.
78. Oda T, Yano M, Yamamoto T, Tokuhisa T, Okuda S, Doi M, Ohkusa T, Ikeda Y, Kobayashi S, Ikemoto N, Matsuzaki M. Defective regulation of interdomain interactions within the ryanodine receptor plays a key role in the pathogenesis of heart failure. Circulation 2005;111:3400–3410.
79. Marx SO, Reiken S, Hisamatsu Y, Jayaraman T, Burkhoff D, Rosemblit N, Marks AR. PKA phosphorylation dissociates FKBP12.6 from the calcium release channel (ryanodine receptor): defective regulation in failing hearts. Cell 2000;101:365–376.
80. Jones JL, Reynolds DF, Lai FA, Blayney LM. Ryanodine receptor binding to FKBP12 is modulated by channel activation state. J Cell Sci 2005;118 (Part 20):4613–4619.
81. Sharma MR, Jeyakumar LH, Fleischer S, Wagenknecht T. Three-dimensional visualization of FKBP12.6 binding to an open conformation of cardiac ryanodine receptor. Biophys J 2006;90:164–172.
82. Trabuco LG, Villa E, Mitra K, Frank J, Schulten K. Flexible fitting of atomic structures into electron microscopy maps using molecular dynamics. Structure 2008;16:673–683.
83. DiMaio F, Tyka MD, Baker ML, Chiu W, Baker D. Refinement of protein structures into low-resolution density maps using rosetta. J Mol Biol 2009;392:181–190.
84. Kimlicka L, Lau K, Tung CC, Van Petegem F. Disease mutations in the ryanodine receptor N-terminal region couple to a mobile intersubunit interface. Nat Commun 2013;4:1506.